Optical microscopy methods for understanding learning and memory

Aditya Singh, Suraj Kumar, Vikram Pal Singh and J. Balaji*

Centre for Neuroscience, Indian Institute of Science, Bangalore 560 012, India

Structural dynamics of dendritic spines is one of the key correlative measures of synaptic plasticity for encoding short-term and long-term memory. Optical studies of structural changes in brain tissue using confocal microscopy face difficulties of scattering. This results in low signal-to-noise ratio and thus limiting the imaging depth to few tens of microns. Multiphoton microscopy (MpM) overcomes this limitation by using low-energy photons to cause localized excitation and achieve high resolution in all three dimensions. Multiple low-energy photons with longer wavelengths minimize scattering and allow access to deeper brain regions at several hundred microns. In this article, we provide a basic understanding of the physical phenomena that give MpM an edge over conventional microscopy. Further, we highlight a few of the key studies in the field of learning and memory which would not have been possible without the advent of MpM.

Keywords: Learning, memory, optical microscopy, two-photon excitation.

SANTIAGO Ramón y Cajal through his neuroanatomical studies using Golgi stain and light microscopy put forth the neuronal hypothesis[1]. Observing the Golgi stained slices of various brain regions (Figure 1), Cajal suggested that the membranous protrusions found on the dendrites of the neuron may serve as the putative sites for synapse formation. He further thought that these protrusions, known as synaptic spines, could be plastic and can possibly serve as information storage sites. However, for a long time it was difficult to demonstrate whether the dendritic spines are plastic. Developments in the field of depth-resolved live cell fluorescence imaging and confocal microscopy made it possible to demonstrate the dynamic nature of the spines[2]. Despite these findings it was not clear if the spines continue to remain dynamic after development and if plasticity-inducing events trigger new spine formation. In order to answer these questions it is necessary to follow the spine dynamics, while such plasticity-inducing changes are occurring in a neuron. Imaging spines present inside a scattering live brain tissue required a technique that is benign and minimally affected by scattering. One of the major limiting factors in addressing this was lack of such microscopic methods to image live brain slices with near-micron resolution. Advent of two-photon microscopy[3] helped overcome this limitation and made it possible to show that the new spines are formed after long-term potentiation (LTP) induction in the CA1 region[4]. In general, the hypothesis of correlation between new spine formation and memory storage has gained favourable evidence[5–8]. Despite these developments, the significance of new spine formation and its contribution to information storage have been debated. Several recent studies utilizing two-photon microscopy of mice cortical regions have established that the spine density is altered following a variety of learning tasks[6,9]. Much of these developments in our understanding of plasticity at the synapse would have been difficult to come by if not for the pertinent developments in optical microscopy. One such development is the use of two-photon microscope to extend the depth of imaging to reach the upper layers of the cortex[10].

Scattering of light by brain tissue limits the imaging depth in light microscopy[11]. Maximal imaging depth, defined as the depth at which the signal generated from the focal volume becomes indistinguishable from the background noise is affected by light scattering[12]. Multiphoton microscopy (MpM) uses multiple photons of lower

Figure 1. Santiago Ramón y Cajal observing brain slices to sketch neuronal structures under bright-field compound microscope.

*For correspondence. (e-mail: balaji@cns.iisc.ernet.in)

energy at high photon density to excite the fluorophore. Multi-photon excitation has several advantages that help extend the maximal depth of imaging. The use of low energy and hence longer wavelength light reduces the loss due to scattering. Apart from this, multi-photon excitation is localized and hence is inherently confocal eliminating the need for depth discrimination on the detector side. This tremendously increases the sensitivity and hence the imaging depth. These factors together made it possible to image and follow the neuronal dynamics of the cortical layers of mice brain *in vivo*. In this article, we will focus on understanding the basic principles of two-photon microscopy, how it compares with its one-photon counterpart and why it is suitable for *in vivo* imaging. We will describe, in brief, some of the latest technological developments and review some of the recent findings that would not have been possible without these developments. The intention of choosing these studies is more towards illustrating what is possible rather than to comprehensively describe what all has been done.

Principle of confocal detection and two-photon excitation

Our ability to follow the dynamics of spines requires that our imaging system is capable of imaging and resolving these structures on the neuron. The volume of the spines increases as they mature and accommodate more post-synaptic density to become functional. During this process, the spines go through various morphological changes leading to a range of shapes and sizes[13]. The volume of a typical mature spine is ~ 1 μm^3. Thus, the optical method used to follow the dynamics of the spines needs to possess near sub-micron resolution in all three dimensions.

Owing to the benign nature of optical microscopy, it has been used to image live tissue. Addition of confocal aperture in such cases helps achieve three-dimensionally resolved images of live tissue through optical sectioning. Confocal detection relies on the ability to discriminate the fluorescence based on its plane/point of origin. The schematic presented in Figure 2 illustrates this principle with a set of minimal optical elements. A parallel beam of excitation light (solid dark green) is reflected by the dichroic mirror onto the back aperture of the objective lens, which focuses the incident beam of light into the sample. As the beam converges into the sample, the molecules present along the path of the incident light get excited and emit fluorescence. The fluorescence light rays are collected back by the same objective lens ('epi detection') and as they emerge out of the objective back aperture, the light rays differ in their convergence. The light rays originating from focus are parallel, whereas the other rays diverge or converge depending on whether they originate between the lens and focus, or beyond the focus. For simplicity, the schematic illustrates the light rays originating from three illustrative planes: (i) dashed lines represent light originating before the focal plane, (ii) solid lines represent light originating at the focus and (iii) dotted lines represent light originating after the focus. The fluorescence light after being collected by the same objective lens passes through the dichroic mirror. Dichroic mirrors are a special type of mirrors which reflect a particular portion of the spectrum while they transmit the other portions. Spectrum of a dichroic mirror along with the excitation and emission spectra of a fluorophore (mOrange) are shown in Figure 2 *b*. The dichroic mirror in this optical geometry is chosen so as to

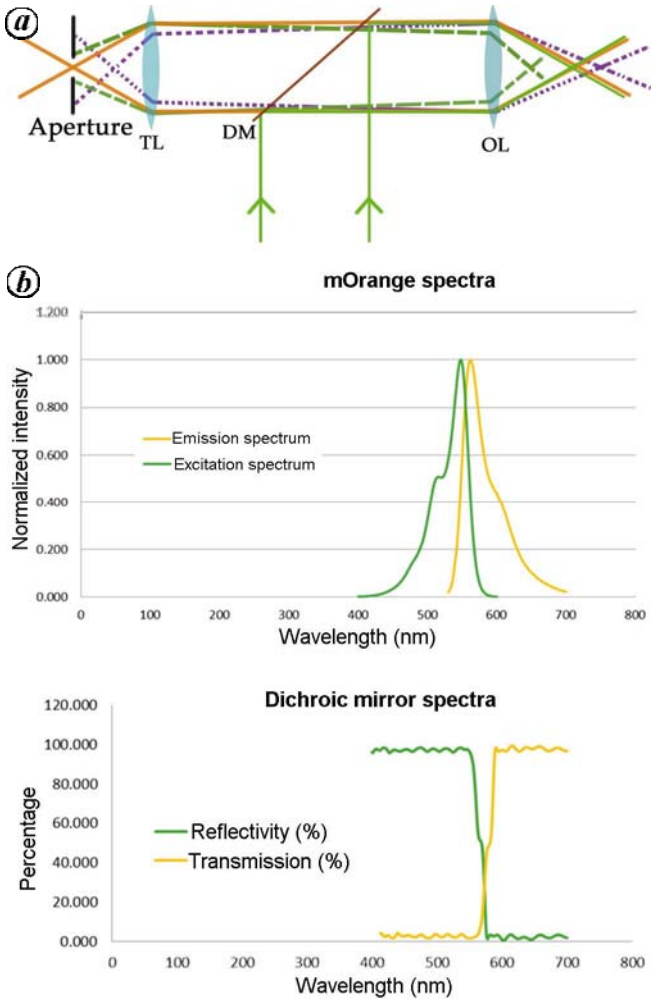

Figure 2. ***a***, Schematics of a confocal microscope. Incident beam (light green) is directed to the sample using a dichroic mirror (DM) and focused by an objective lens (OL). Fluorescence (dark green/dashed, orange/solid, and purple/dotted) is generated from the sample throughout the incident beam path. Longer wavelength fluorescence gets through the DM to focusing lens (TL). An aperture placed at the focal plane of TL selects fluorescence from OL focus plane (orange/solid), and blocks all other out-of-focus fluorescence (dark green/dashed, purple/dotted). ***b*** (Top), Dichroic mirror spectrum showing transmitted and reflected wavelengths. Normalized excitation and emission spectra of mOrange are shown below. (Bottom) The dichroic mirror can be used for both reflecting the excitation wavelengths to excite mOrange and transmitting the emitted fluorescence from mOrange.

reflect the lower wavelength excitation light while transmitting the higher wavelength emission light. The collected light after passing through the dichroic mirror gets focused by a collection/tube lens. From the ray diagram, it can be clearly seen that the fluorescence originating from three different points in the sample has corresponding planes of focus. These sets of points represent the conjugate object and image planes. A pinhole placed at the conjugate plane of the objective focus would obstruct most of the out-of-focus light to reach the detector, while leaving most in-focus light to pass through, as illustrated in Figure 2 *a*. This results in a differential detection of fluorescence at the detector based on the plane of origin leading to depth resolution in confocal microscopy.

Confocal detection overcame the limitations of imaging techniques such as electron microscopy, PET and MRI by enabling three-dimensional imaging in live tissue with subcellular resolution. However, confocal microscopy is limited when it comes to imaging live brain tissue. The inhomogeneous refractive index of the brain tissue presents a huge challenge to confocal microscopy. Due to such tissue profile, desired photons from the focal plane are scattered away from the pinhole and undesirable photons from other focal planes peek in, resulting in loss of signal-to-noise ratio. Further, the large excitation volume induces phototoxicity and photobleaching.

Two-photon microscopy

In optically thick scattering tissue such as brain, discriminating the out-of-focus light using a pinhole results in greater reduction of signal and this limits the maximal depth of imaging. Use of longer wavelength light and inherently localized nature of excitation in two-photon microscopy help overcome this problem. In two-photon microscopy, high density of low energy (roughly half that of the energy gap) and hence longer wavelength of photons are focused onto the sample. Under such conditions, the fluorophores have a very low probability of reaching the excited state by absorbing two of these light photons quasi-simultaneously. Since the molecules need to absorb two light photons simultaneously, this absorption has a quadratic dependence on intensity (eq. (3)). Figure 3 illustrates the process of two-photon absorption against the one-photon excitation using energy-level diagrams. A fluorophore with an energy gap (ΔE) corresponding to an excitation wavelength of λ_{ex} ($= hc/\Delta E$), can reach the excited state by absorbing either one of the energy-matched light photons of wavelength λ_{ex} or two photons of half the energy and hence twice the wavelength. The process of absorbing multiple photons to reach an excited state was predicted by Maria Goeppert-Mayer. However, to realize the potential of such a low probable phenomenon, very high intensities of light were needed. Pulsed lasers with their ability to generate intense light for brief periods of time made that realization possible. A rigorous treatment of the process of two-photon absorption itself is beyond the scope of this article. One of the simpler ways of understanding two-photon absorption is through consideration of energy–time uncertainty relation

$$\Delta E \cdot \Delta t \geq \frac{\hbar}{2}. \tag{1}$$

In essence, the uncertainty principle predicts that energy accuracy comes at the cost of uncertainty in time and vice versa. Thus, for energy gaps corresponding to the visible excitation/electronic level transition, we have

$$\Delta t \geq \frac{\hbar}{2 \cdot \text{Energy gap}}. \tag{2}$$

Thus it is possible to introduce the idea of short-lived intermediate state through which two-photon absorption can take place. The lifetime of such a state would be limited by ΔE as given by eq. (2). This corresponds to 10^{-1}–10^{-2} fs for electronic transitions[14]. Such a picture is inadequate and gets more complex when it comes to explaining higher-order processes such as three-photon absorption.

Localized nature of two-photon excitation

Gaussian laser beam when focused through a lens, in combination with quadratic dependence of two-photon

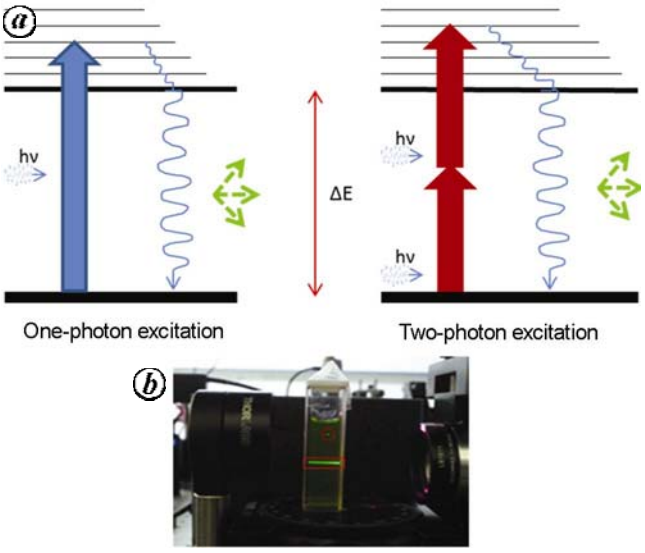

Figure 3. ***a***, Two-photon excitation involves absorption of two photons of half the energy to excite a molecule (top right). ***b***, The two-photon excitation process results in fluorescence originating only from the focus (red circle) where a high number of photons is restricted to a small volume. One-photon absorption due to continuous wave laser excites almost all the fluorophores in the path (red rectangle) resulting in low signal-to-noise ratio and low z-axis resolution compared to two-photon absorption.

absorption on incident intensity causes the excitation probability to fall rapidly around the focus. In the following section, we compare and contrast one-photon and two-photon absorptions and bring out the salient features of these processes.

The molecular rate of excitation and hence the resulting fluorescence is linearly dependent on the intensity of the incident light for one-photon excitation, while it has a quadratic dependence in case of two-photon excitation. This is the probability per unit time that the incident light will interact with the molecule and excite it to the next electronic state.

In general, these rates can be written as

$$\text{Molecular rate of } n \text{ photon excitation } (R^{\text{np}}) = \sigma_{\text{np}} \cdot I_{\text{np}}^{n}, \tag{3}$$

σ_{np} is the n photon absorption cross-section and I_{np} is the intensity of the incident light (no. of photons/area·time).

For one-photon and two-photon processes n can be and 1 and 2 respectively.

These rates being a measure of probability of excitation have a maximal saturating value of unity. In case of the two-photon process, the proportionality constant $\sigma_{2\text{p}}$ is the molecular two-photon absorption cross-section analogous to $\sigma_{1\text{p}}$ its one-photon counterpart. $\sigma_{1\text{p}}$ is related to the more familiar molar absorption coefficient ε through Avogadro constant (N_{A}) as $N_{\text{A}}\sigma_{1\text{p}}$. Table 1 lists the cross-sections for some of the commonly used fluorophores[15]. The low probable nature of two-photon absorption is reflected in the difference in magnitudes of the one- and two-photon absorption cross-sections. These cross-sections determine the intensity at which saturation occurs.

The two-photon absorption cross-section being considerably lower than its one-photon counterpart, the intensity required to saturate is considerably higher. Such high intensity of incident light is achieved through the use of pulsed lasers. This is done to keep the average intensity (per unit time) low, especially so when it comes to imaging live biological tissue. In a pulsed laser, the photons are bunched in time. Representing these pulses as periodic Gaussian peaks with a width of τ_{p} and inter-pulse separation of τ_{r} (Figure 4), we relate the peak and average intensities.

Thus,

$$\text{Average intensity } (I_{\text{avg}}) = \frac{\tau_{\text{p}}}{\tau_{\text{r}}} \times \text{peak intensity } (I_{\text{peak}}) \times s_{\text{f}},$$

where τ_{p} is the pulse width, τ_{r} the inter-pulse separation (1/repetition·rate) and s_{f} is the scaling function.

Rearranging for I_{peak},

$$I_{\text{peak}} = \frac{\tau_{\text{r}}}{\tau_{\text{p}}} \times s_{\text{f}} \times I_{\text{avg}}. \tag{4}$$

In eq. (4), the scaling function accounts for the fact that the actual pulse shape is not rectangular. Thus, it is the ratio of areas of the pulse shape with a width τ_{p} (defined as distance between the points where intensity drops to $1/e^2$ of I_{peak}) and height I_{peak} (Figure 4), to that of a rectangle with a width τ_{p} and height I_{peak} (Figure 4). For a Gaussian pulse, scaling function is given by

$$s_{\text{f}} = \frac{\int_{-\infty}^{\infty} I_{\text{peak}} \cdot \text{e}^{-2t^2/\tau_{\text{p}}^2}}{I_{\text{peak}} \cdot \tau_{\text{p}}} \approx 0.6. \tag{5}$$

Using the above relationship one can rewrite eq. (3) as follows

$$\left.\begin{array}{l}\text{Probability of excitation (per pulse)}\\ \text{for the } n \text{ photon process}\end{array}\right\} \theta^{\text{np}} = \sigma_{\text{np}} \cdot I_{\text{peak}}^{n}, \tag{6}$$

$$\left.\begin{array}{l}\text{Rate of excitation}\\ \text{(per unit time)}\end{array}\right\} R^{\text{np}} = \sigma_{\text{np}} \cdot I_{\text{peak}}^{n} \cdot \frac{\tau_{\text{p}}}{\tau_{\text{r}}}. \tag{7}$$

Using eq. (3) and eq. (4) we get

$$R^{\text{np}} = \sigma_{\text{np}} \cdot \frac{I_{\text{avg}}^{n}}{s_{\text{f}}^{n}} \cdot \frac{\tau^{n-1}}{\tau_{\text{p}}^{n-1}}, \tag{8}$$

where σ_{np} is the absorption cross-section and I is the intensity of the incident light (no. of photons/area · time).

Thus, the use of ultra-short pulses and narrowing the pulse width greatly help increase excitation rate for a given average power. While the use of ultra-short pulses makes two-photon excitation possible, the inherent nonlinearity of the two-photon excitation itself gives rise to spatial localization.

Using cylindrical coordinates, intensity profile of the laser beam that is focused through a lens along sample depth (z) is given by

$$\text{Intensity } I(r, z) = I_0(z) \cdot \text{e}^{-2r^2/\omega_z^2(z)}, \tag{9}$$

where $I_0(z) \rightarrow I(r = 0, z)$, i.e. intensity at the centre of the beam at a given z,

$$\omega_z^2 = \omega_0^2 \left(1 + \left(\frac{\lambda z}{\pi \omega_0^2}\right)^2\right), \tag{10}$$

ω_0 is the spot size at focus = $\lambda/(\pi \cdot NA)$, λ is the wavelength and NA the numerical aperture of the lens.

However, for high-resolution optical imaging we are typically operating close to the diffraction limit. Therefore eq. (10) has to be treated as an approximation to the actual spot size since the Gaussian description is not valid

Table 1. One-photon (1p) and two-photon (2p) absorption cross-sections (σ) at respective wavelengths (l_{max}) for some common fluorophores[32]

Fluorophore	l_{max} (1p) nm	σ_{1p} (cm^2) × 10^{-16}	l_{max} (2p) nm	σ_{2p} (GM)
DAPI	345	1.3	700	102
Alexa 488	494	2.8	760	95.62
Fluorescein	490	2.6	770/780/790	37.33*
Alexa 594	590	3.5	780	99.8
eGFP	489	2.1	942	184.1
DsRed	558	2.4	990	108.87 (SD = 0.93)*

*SD, standard deviation in measured 2pσ for fluorescien at different l_{max}.

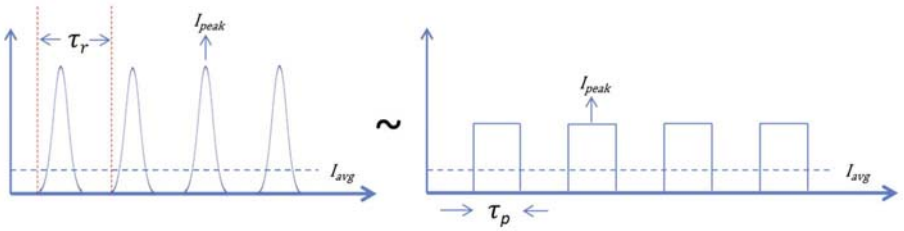

Figure 4. In case of a pulsed laser with peak intensity, I_{peak} each pulse has a very large number of photons bunched together in a short time-window. Inter-pulse separation, τ_r, corresponds to the time it takes for a pulse to complete one round trip within the laser cavity. Approximation of Gaussian pulses to rectangular pulses is shown on the right.

in such cases. Further, it is customary to normalize the intensity profile such that the rate of excitation is unity at the focus. The rationale being that at the focus, the rate of excitation is the highest and the maximal achievable rate of excitation (eq. (7)) is 1.

An interesting corollary to this is saturation intensity given by

$$\text{Setting eq. (8) to 1} \Rightarrow I_{sat}^{n} = \frac{\tau_p^{n-1} \cdot s_f^{n}}{\sigma_{np} \cdot \tau_r^{n-1}}. \quad (11)$$

Using this to normalize eq. (8) and using eq. (9) to express $I(0, z)$, we have,

$$\text{Intensity profile } I(r, z, \omega_z) = I_{sat} \cdot \frac{e^{-2r^2/\omega_z^2}}{\int_{-\infty}^{\infty} e^{-2r^2/\omega_z^2} dr}$$

$$= I_{sat} \cdot \frac{e^{-2r^2/\omega_z^2}}{\omega_z \sqrt{\pi/2}}. \quad (12)$$

The excitation beam profile (Figure 5) is characterized by the wavelength of light that is being focused and the numerical aperture of the lens. It is evident from eq. (10) that the radial dimension of the smallest spot at the focus and hence the lateral resolution are dependent on the wavelength of the excitation light. Typically the wavelength of light used for two-photon excitation is larger than that of one-photon excitation. As a result it is often suggested that spot size and hence the resolution of the two-photon process is poor compared to the one-photon. However, we will proceed to show why such a conclusion is misleading and often incorrect.

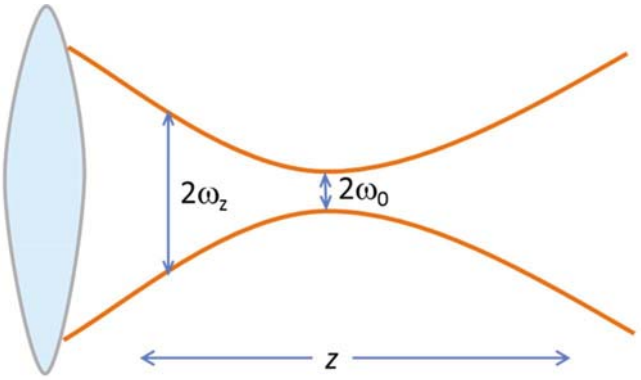

Figure 5. Gaussian beam focus: Beam width at focus ($2\omega_0$) is the minimum achievable beam diameter after focusing through a lens. $2\omega_z$ represents beam at distance Z from focus. At focus, $Z = 0$.

The spatial variation of the excitation rate or the excitation point spread function (PSF) for one-photon and two-photon excitation can be obtained from their beam profiles. Equation (8) represents the probability that a molecule in a given (r, z) can get excited, or in other words the excitation PSF of an 'nth' order excitation process. Writing these explicitly for the one- and two-photon processes we have using eqs (8), (11) and (12)

One-photon process Two-photon process

$$R^{1p} = \frac{e^{-2r^2/w_z^2}}{\sqrt{\pi/2} \cdot w_z} \qquad R^{2p} = \left(\frac{e^{-2r^2/w_z^2}}{\sqrt{\pi/2} \cdot w_z} \right)^2. \quad (13)$$

In arriving at the above equations, we have assumed that the wavelength of excitation for two-photon excitation is

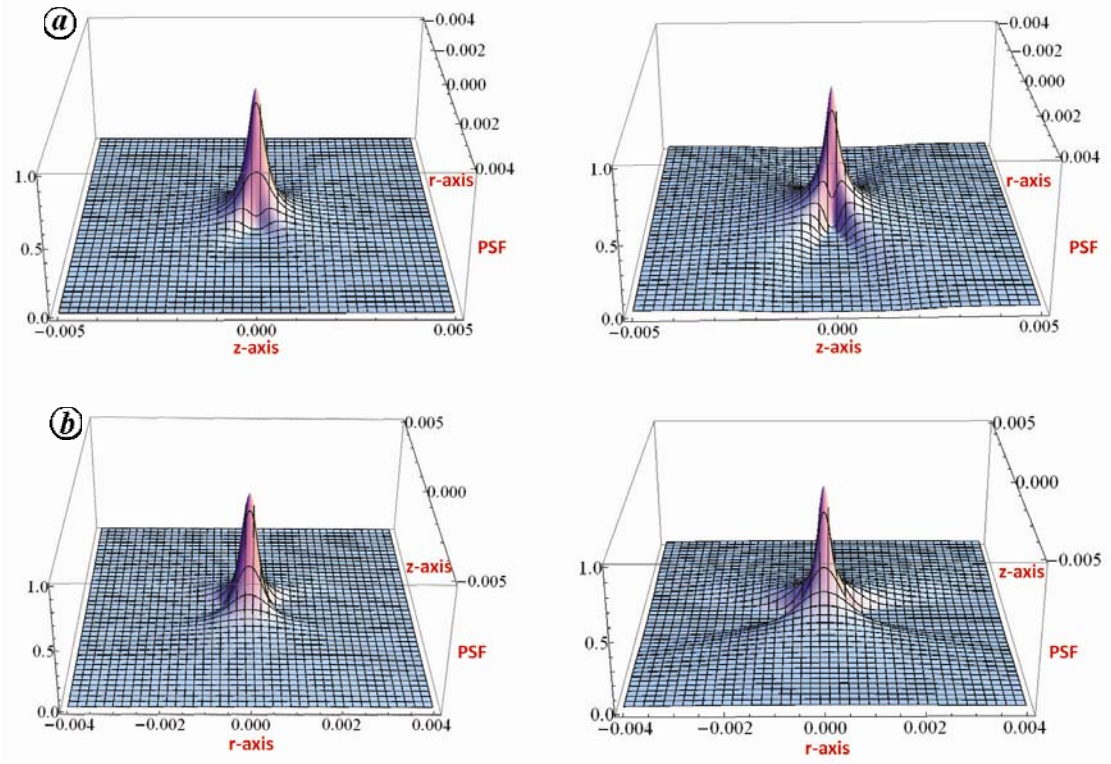

Figure 6. Normalized profiles of excitation rates for two-photon (left) and one-photon excitation (right) as a function of space. Broader point spread function (PSF) is observable in two-photon excitation at the start; however, it falls more rapidly outside focus when compared to one-photon profile. The radial and axial views are provided in the top and bottom panels. Numerical values depict distance from focus in micrometres.

twice that of one-photon excitation. Although the excitation wavelength and hence the spot size are larger for the two-photon process, the dependence on intensity is quadratic and hence the excitation profile falls more rapidly for the two-photon process. Thus the spot size by itself does not correspond to the resolution here, as the probability of excitation has a quadratic dependence on intensity. In order to understand how the excitation probability is distributed in space for one- and two-photon excitation, we plot these against spatial coordinates (Figure 6). In order to obtain these plots we have assumed that the two-photon excitation wavelength is twice the one-photon excitation. However, it is often smaller than twice the one-photon excitation wavelength. This would diminish the difference in focal spot size.

Although the PSF for one-photon excitation is narrower at the focal spot (due to smaller wavelength), the two-photon PSF decreases faster. As a result, the one-photon PSF is substantially spread outside of the focal spot compared to the two-photon PSF. This becomes more evident when we look at the difference profiles of these two PSFs (Figure 7). Thus, even though the spot size is smaller, the overall excitation profile and hence the excitation PSF for one-photon PSF are larger than the two-photon PSF. This renders the two-photon excitation an increased ability to localize the fluorescence to the focal spot.

Another factor that contributes heavily for spatial localization is the out-of-focus fluorescence. This is often well illustrated in a simple demonstration such as the one shown in Figure 3. Such a striking difference could not be explained only by considering the PSFs. The PSF determines photon density across space and hence the probability that a given fluorophore will get excited at that space. However, the fluorescence is dependent on this and is also proportional to the number of fluorophores per unit excitation volume. Thus to get the fluorescence profile from the PSF, we need to account for the change in the density of the fluorophores. As the beam size varies, the number of fluorophores available for excitation also varies. When we take this factor into account we have

Fluorescence rate,

$$f^{\mathrm{np}} = R^{\mathrm{np}} \cdot \frac{\int_{-\infty}^{\infty} \mathrm{e}^{-2r^2/w_z^2} \cdot \mathrm{d}r}{\int_{-\infty}^{\infty} \mathrm{e}^{-2r^2/w_0^2} \cdot \mathrm{d}r} = R^{\mathrm{np}} \cdot \sqrt{1+\left(\frac{\lambda_{\mathrm{np}} \cdot z}{\pi \cdot (\lambda_{\mathrm{np}}/\pi \cdot NA^2)}\right)^2}. \quad (14)$$

The plot of eq. (14) generates the expected fluorescence profile for both one- and two-photon excitation. It is shown alongside the measured profile of the image (Figure 8). It should be noted that such a vast difference in its extent of spatial localization does not limit the use of one-photon excitation for optical sectioning in confocal microscopy. The lateral resolution in such cases is achieved by the use of a pinhole to reject the out-of-focus light.

Optical schematic of two-photon microscope

Two-photon microscope makes use of the inherent localized nature of excitation discussed above to create a high-resolution representation of the live sample that is being imaged. This is achieved through simultaneous raster scanning of the sample being imaged and recording of the two-photon induced fluorescence at each point as the beam is scanned.

The optical set-up of a two-photon microscope system consists of an ultrafast femtosecond system as the light source, a laser scanning system based either on galvanometric mirrors or acousto-optic deflectors, microscope body frame, objective lens and photomultiplier-based detection system. The ultrafast laser system is usually a Ti : sapphire-based mode-locked IR laser. Ti : sapphire crystal has a wide gain bandwidth and hence wide tuning range of ~ 680–1080 nm. In a typical set-up it is pumped by intra-cavity doubled 532 nm Nd : YAG laser or its variant. The infrared output generated from such a Ti : sapphire laser system is directed into a prism pair dispersion compensator unit and a beam intensity modulator before entering the scan assembly. In the scan assembly the beam is raster scanned in orthogonal axis which is then imaged onto the back of the objective lens. The objective lens then focuses the beam onto the sample to excite fluorescence which is then collected back by the same objective lens before getting reflected onto a photomultiplier tube (PMT) by a dichroic mirror placed right beneath the objective lens. The schematic of a typical two-photon microscope set-up is shown in Figure 9.

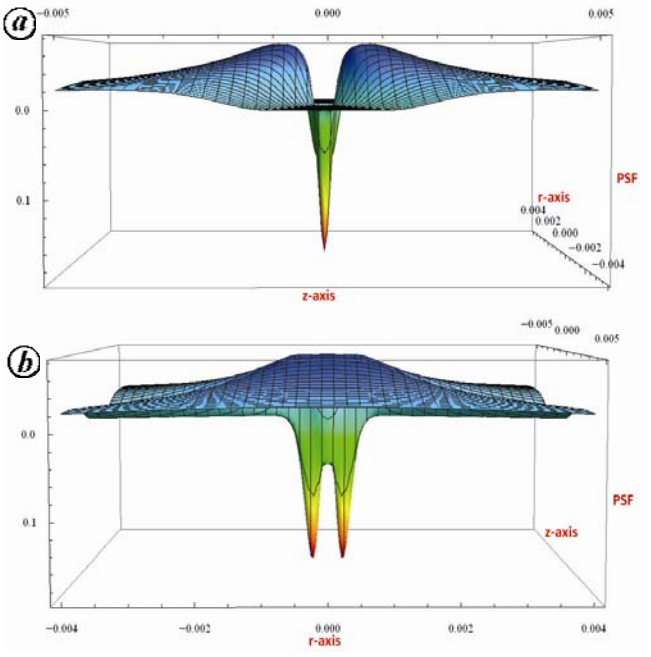

Figure 7. Difference between PSFs during one-photon and two-photon excitation. ***a***, Along the *z*-axis, net rate/probability of excitation is evident after $PSF_{1p} - PSF_{2p}$. ***b***, $PSF_{1p} - PSF_{2p}$ when observed along the *r*-axis. The central peak is due to the difference in spot size and the out-of-focus negative regions are due to the slow decline of one-photon PSF compared to two-photon PSF.

Measuring pulse width and compensating for dispersion

The amount of fluorescence generated at saturating intensity of incident light beam determines the signal-to-noise ratio in a two-photon image. Equation (11) predicts that this fluorescence intensity at saturation is inversely proportional to the pulse width for a given average energy. It is important to keep the average energy low to minimize the photodamage and other phototoxicity effects. This is achieved through the use of ultra-short femtosecond pulses. Depending on pulse width, one ultra-short pulse can include a range of wavelengths around the desired central wavelength. This can be seen as a consequence of Heisenberg's uncertainty relation that we considered earlier. However, in this context ΔE would denote the energy difference between the lower (λ_l) and higher wavelengths (λ_u) of the pulse bandwidth and Δt represents the transform-limited pulse width. That is,

$$\Delta E_{\text{bandwidth}} \cdot \Delta t_{\text{pulse width}} \geq \frac{h}{2\pi}.$$

Using Planck's equation ΔE can be written as

$$\Delta E = hc\frac{(\lambda_{\text{u}} - \lambda_{\text{l}})}{\lambda_{\text{l}}\lambda_{\text{u}}}$$

$$\cong hc\frac{\Delta\lambda}{\lambda^2_{\text{centre}}}$$

Thus we have

$$\Delta\lambda \geq \lambda^2_{\text{centre}}\left(\frac{1}{2\pi c\Delta t}\right).$$

As refractive index is a function of the wavelength of light for a given medium, different wavelengths suffer different amounts of phase delay. Thus, after multiple

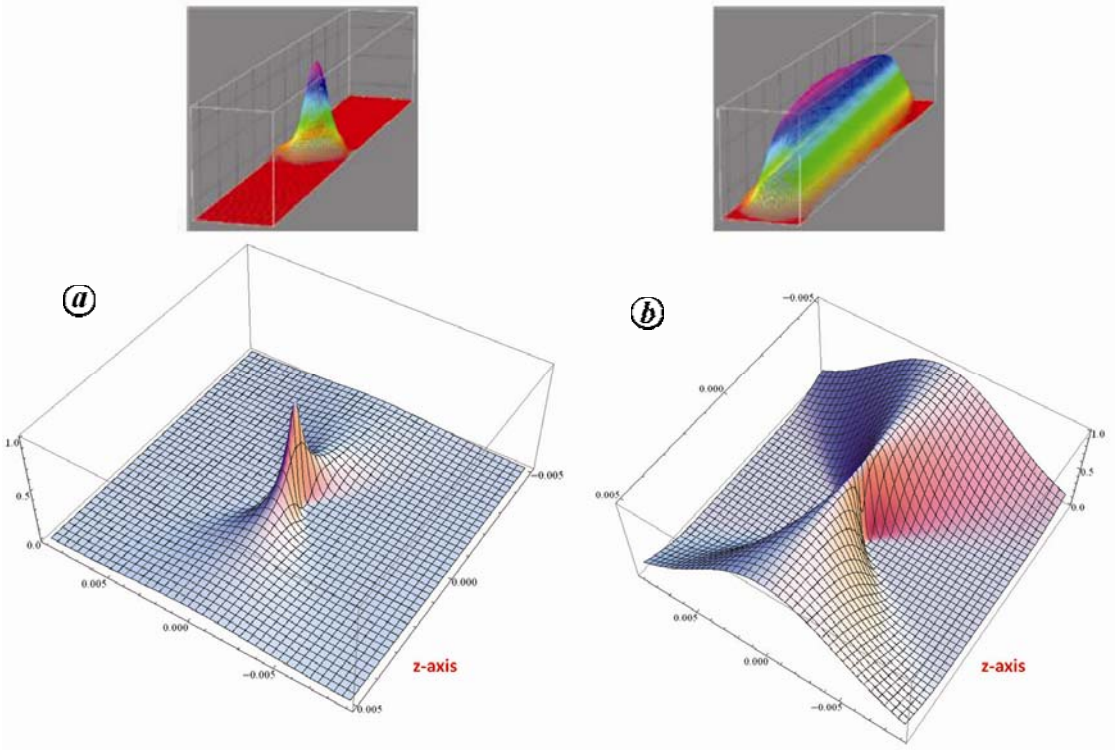

Figure 8. Fluorescence profile illustrating the combined effect of loss in number of available fluorophore molecules and gain in photon density as a result of focusing. Actual image profile is shown on the top. ***a***, During two-photon excitation the spatial localization is achieved as the gain due to increased photon density is quadratic. ***b***, One-photon excitation. All planes along the focus contribute equally as the loss in the number of molecules due to spatial localization is exactly offset by the gain in photon density.

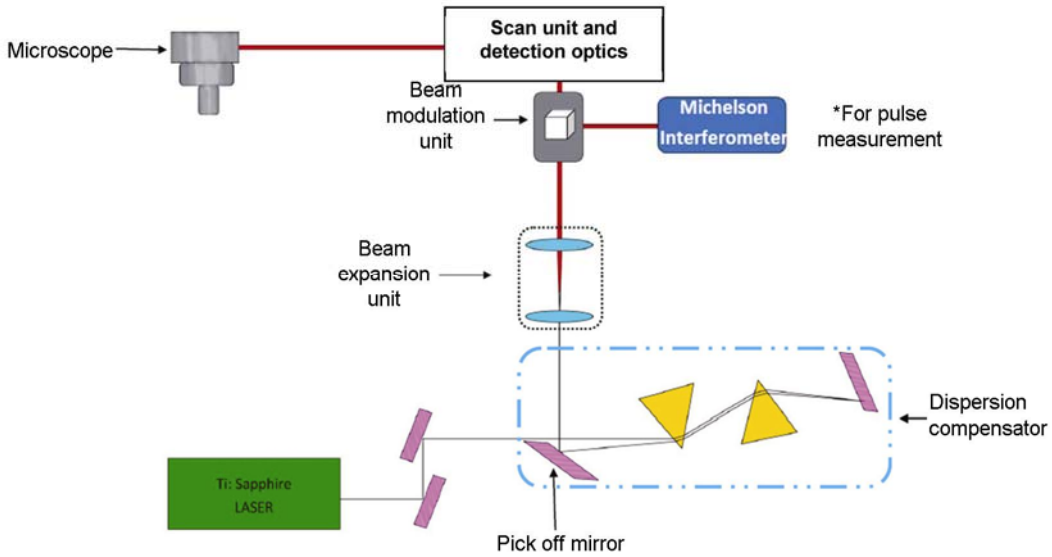

Figure 9. Optical set-up illustrating components of a two-photon microscope. Incident Ti : sapphire laser is pre-chirped to compensate for effect of dispersive elements in the optical path. Pre-chirped pulse is expanded to sufficiently fill the back aperture of the objective lens. Michelson interferometer measures pulse width of incident pulse.

passes through optical components, shorter wavelength component of a pulse gets slowed down more compared to the longer wavelength component. Due to this process, wavelength-dependent dispersion in a medium renders the original pulse stretched in time domain. Such a stretched pulse is known as 'chirped pulse'. The effect of this differential phase delay among the wavelength components is to widen the pulse. Thus a 100 fs pulse originating from the laser gets widened due to dispersion after it passes through various optical elements in the path,

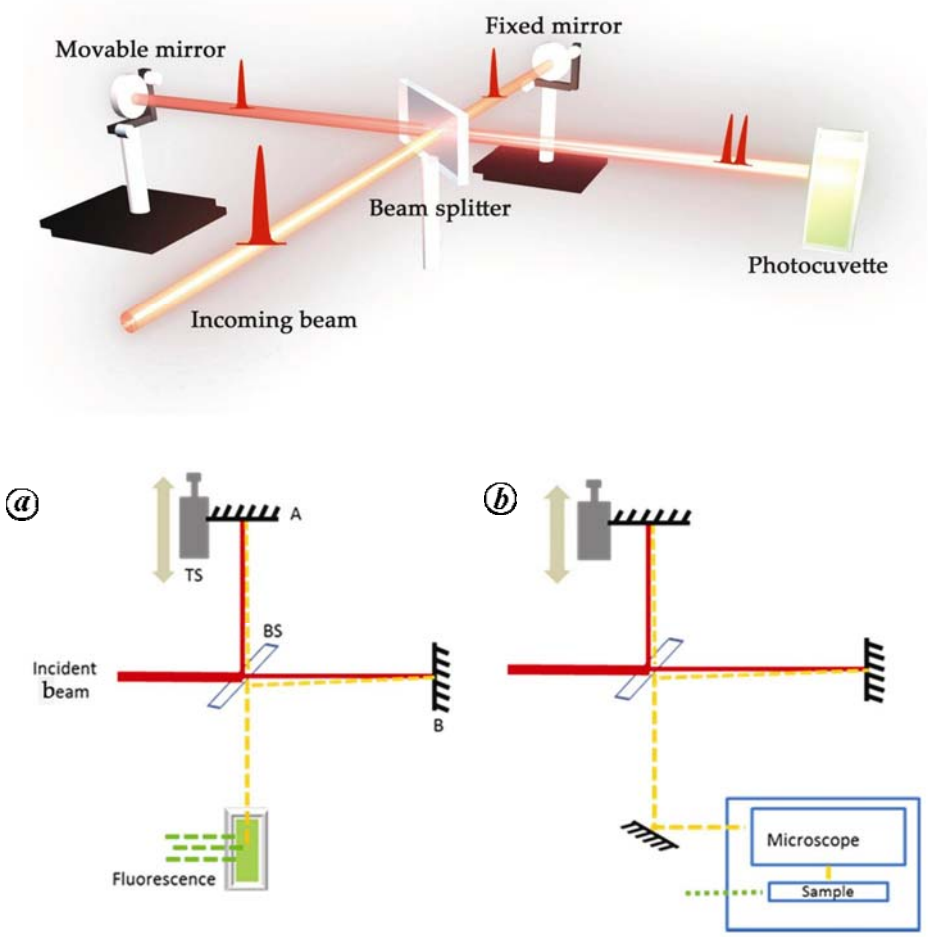

Figure 10. (Top) Optical set-up illustrating components of Michelson interferometer (MI). Schematic showing the implementation of MI for measuring pulse width before (***a***) and after (***b***) the objective lens to estimate the amount of dispersion caused due to optical components.

including the high-NA objective lens. As a result it is important to measure the pulse width at the sample so as to optimize the signal-to-noise ratio of two-photon images. Typical pulse measurements are made outside of the microscope owing to the cumbersome optics involved and physical inability to mount them at the focal plane of the objective lens. Here we illustrate the use of modified Michelson interferometer (MI) to measure pulse width at the sample.

The set-up for MI (Figure 10) consists of two mirrors placed perpendicular to each other. A beam splitter is placed at the point of intersection of the surface normal drawn on the mirrors. This results in the incoming pulse of light being spilt into two arms with the intensity of the arms dictated by reflectance/transmittance ratio of the beam splitter. These pulses being normally incident on the equidistant mirrors situated orthogonally at distance L from beam splitter get reflected back such that the two reflected beams are spatially overlapping and travelling in a direction perpendicular to the original incoming beam. This outgoing beam then enters the detection system. The difference introduced in length of the two arms by moving one of the orthogonal mirrors, introduces a temporal separation between the two pulses that are spatially overlapped. The temporal separation for a small difference (Δl) in the two arms of total length L mm is given by

$$\text{The difference between arrival of two pulses at the detector } (\tau) = \frac{\Delta l}{c}.$$

Thus by varying one of the arm lengths in the interferometer, the temporal separation and hence the extent of temporal overlaps between the pulses can be varied. Pulse width is measured through an auto-correlation measurement by translating one of the pulses with respect to the other by varying the degree of temporal overlap, as illustrated in Figure 10. Such a translating arrangement when combined with a nonlinear integrator/detector makes it possible to measure the pulse width. In our case we use two-photon excitation-induced fluorescence as a nonlinear integrator.

Prism pair compensator

Measuring the pulse width at the sample using MI allows estimation of dispersion associated with the pulse. The dispersion can be compensated using a pair of high refractive index prisms. The first prism disperses the wavelength components in space while second prism, placed in an inverted orientation relative to the first, introduces a linearly increasing delay across the wavelength. This is accomplished as the thickness of the prism increases from tip to base and the pulse is spatially dispersed along the side of the prism. This selectively slows down longer wavelengths relative to the shorter wavelengths, resulting in a negative chirp. When the amount of this negative chirp is matched to compensate for the dispersion in the microscope set-up, the pulse width at the source is restored at the sample. The auto-correlation response measured using the set-up before and after the compensation is shown in Figure 11. The corresponding pulse widths estimated from the FWHM of the Gaussian fit to the measured data are ~ 71 and ~ 39 fs respectively.

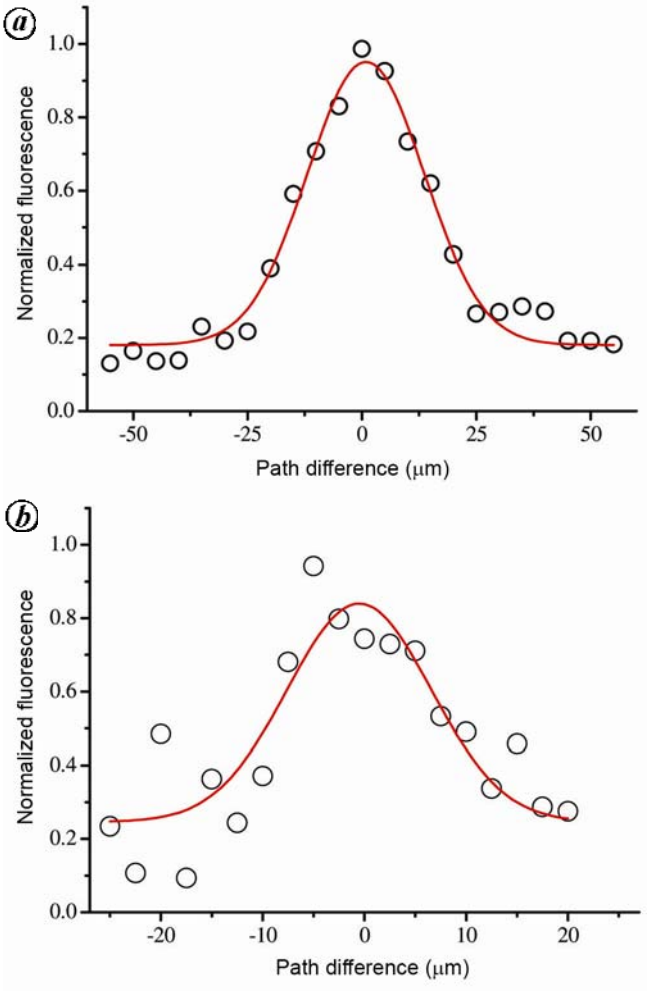

Figure 11. Normalized auto-correlation response measured through a modified Michelson Interferometer before (***a***) and after (***b***) dispersion compensation through a pair of prisms.

Advances in neuroscience by multiphoton microscopy

Structural changes in dendritic spines have been proposed to be a correlate for storing information. One of the limiting factors in testing that was the inability to visualize the submicron changes as they happen in live tissue. Two-photon microscopy helps establish a causal link between long-term potentiation and corresponding structural variations in dendritic spines. It helped in the visualization of changes in the spines of the CA1 pyramidal neurons[4] in response to LTP in organotypic cultures. The advent of two-photon microscopy made imaging of spines in such studies possible. However, a large number of neurons get activated due to such electrical stimulation and thus it is difficult to specifically induce LTP and study the contribution of specific synaptic connections. Matsuzaki *et al.*[16] took advantage of better focusing property of two-photon microscopy for observing spine dynamics in response to more specific inputs. They activated a single spine by local uncaging of glutamate and then imaged the corresponding structural dynamics specifically in those spines by two-photon microscopy. The changes in dendritic protrusions corresponding to spines around the uncaged regions could be seen. Initial studies such as these were being performed either in slices or organotypic cultures using LTP as a representative of learning-induced plasticity *in vitro*.

Later by combining craniotomy with two-photon microscopy, Trachtenberg *et al.*[6] established a more convincing evidence for considering structural changes in spines as a substrate for retention or elimination of information. In transgenic mice having Thy1-promoter mediated GFP expression, they trimmed alternate whiskers to observe input-specific changes in spine dynamics. The corresponding dendritic arborizations where situated deep inside the mice brain at layer-V pyramidal neurons of the barrel cortex. These spines that were > 500 μm deep inside the mice barrel cortex were followed *in vivo*. Using two-photon microscopy *in vivo* in conjunction with serial section electron microscopy post-mortem, they were able to conclude that experience dependent changes in spine number correspond with synapse formation or elimination in adult brain. Consecutive developments in MpM to increase the depth of imaging in highly scattering tissues established it as an efficient tool to explore structural dynamics of neurons in response to learning and memory[17–19].

Apart from aiding cellular and network-level interrogations about brain function[20], MpM also helped answer critical questions about molecular mechanisms related to learning and memory. In the field of learning and memory, one of the intriguing questions is how the strengthening

of a synapse following plasticity affects the neighbouring synapse. Harvey *et al.*[21] using MpM-based lifetime imaging and glutamate uncaging, showed that induction of LTP selectively and locally in one of the synapses reduces the threshold for LTP in the neighbouring spines. For this study they had to rely on the ability of two-photon excitation to image through scattering organotypic slices with subcellular resolution. Further, they made use of the localized nature of this excitation to induce LTP specifically in the dendritic spines and not in its neighbours with sub-micron specificity. They found that lowering of LTP threshold in neighbouring spines happens by Ras-diffusion. Similar fluorescence lifetime imaging microscopy was used to study the roles of actin cytoskeleton maintaining GTPases of Rho family, RhoA and Cdc42, in relaying spine-specific CaMKII activation to long-term structural plasticity at dendritic spines[22]. They used FRET pair of enhanced green fluorescence protein (eGFP) and mCherry to tag GTPases and GTPase-binding domains of Rhotekin/Pak3 respectively. Using two-photon glutamate uncaging, spines were activated and fluorescence from FRET-pairs revealed that RhoA diffuses a few micrometres around the activated spine and Cdc42 fluoresces only near the spine neck, showing differential migration properties and site-specific roles of these GTPases in maintaining long-term synaptic plasticity. On the other hand, Lee *et al.*[23] showed that CaMKII activation in response to short pulses of two-photon glutamate uncaging in hippocampal slices is restricted to only stimulated spine. Using the changes in fluorescence lifetime of GFP-Camuiα FRET-pair attached to CaMKIIα, they could visualize transient and stable changes in spine size after glutamate stimulation. These studies helped conclude that CaMKII might be a principal regulator for specific activation of synapses in response to local inputs at individual spines.

Deep tissue imaging has the ability to track single neuron activity in an intact live animal. However, some of the questions in neuroscience require investigation of animals that are fully conscious, awake and performing a task. Imaging the brain in a freely moving mouse is hard and involves mounting miniaturized optics on the mouse head[24–26]. Lately such miniaturized endoscopes have been used to follow the ensemble neuronal activity during spatial navigation. However, this is still instrumentation intensive per mouse and hence restricted in its ability to be used in studies involving a large group of animals. Emergence of virtual reality and using a head-fixed mouse under the conventional two-photon microscope have opened new avenues.

This set-up includes head-restrained mouse being fixed onto a treadmill (Styrofoam ball), which can move freely in any direction and a wide toroidal screen in front illuminated with a projector (Figure 12). The virtual system uses the movement of mouse, registered through the movement of the Styrofoam ball to process the visual scenes and project them on the screen. Using such a setup it has been possible to study the calcium responses of individual neurons in an ensemble as the animal navigated in space[27–31].

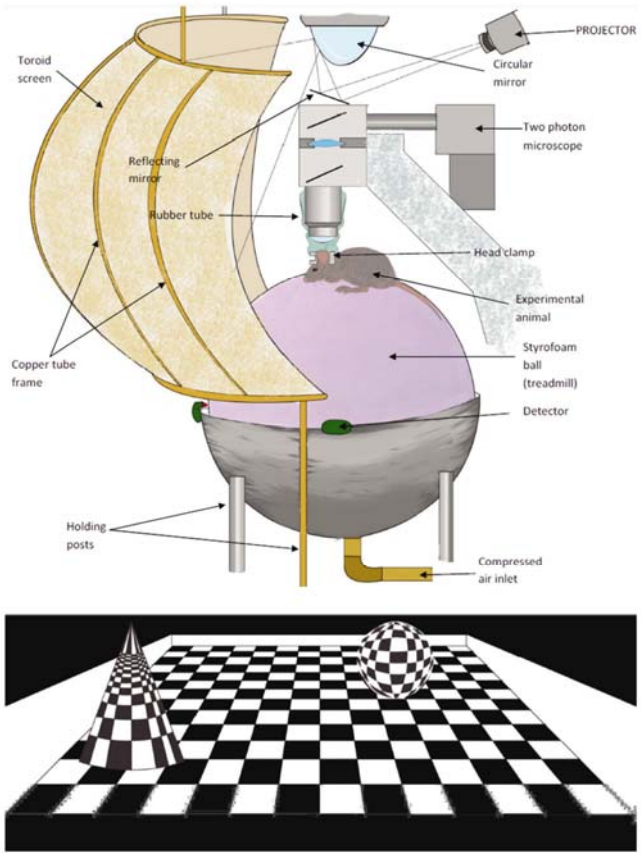

Figure 12. Virtual reality set-up for *in vivo* imaging in mice during virtual explorations. Interactive virtual environment (bottom) is projected on a toroid screen through a reflecting mirror and circular mirror. Mice is held under two-photon microscope using head clamp on top of a styrofoam ball. While the mouse explores virtual environment, the ball functions like a treadmill and keeps floating in a hollow cavity filled with compressed air. Directional components of the moving ball are fed back to the virtual environment using two perpendicularly placed optical mice.

1. Ramón y Cajal, S., Sobre las fibras nerviosas de la capa molecular del cerebelo. *Rev. Trimestral Histol. Normal Patol.*, 1888, **2**, 33–49.
2. Woolley, C. S., Gould, E., Frankfurt, M. and McEwen, B. S., Naturally occurring fluctuation in dendritic spine density on adult hippocampal pyramidal neurons. *J. Neurosci.*, 1990, **10**(12), 4035–4039.
3. Denk, W., Strickler, J. H. and Webb, W. W., Two-photon laser scanning fluorescence microscopy. *Science*, 1990, **248**(4951), 73–76.
4. Engert, F. and Bonhoeffer, T., Dendritic spine changes associated with hippocampal long-term synaptic plasticity. *Nature*, 1999, **399**(6731), 66–70; http://-dx.doi.org/10.1038/19978.
5. Yuste, R. and Denk, W., Dendritic spines as basic functional units of neuronal integration. *Nature*, 1995, **375**(6533), 682–684; http://dx.doi.org/10.1038/-375682a0.
6. Trachtenberg, J. T., Chen, B. E., Knott, G. W., Sanes, J. R., Welker, E. and Svoboda, K., Long-term *in vivo* imaging of

experience-dependent synaptic plasticity in adult cortex. *Nature*, 2002, **420**(6917), 788–794; http://dx.doi.org/10.1038/nature01273.
7. Holtmaat, A., Wilbrecht, L., Knott, G. W., Welker, E. and Svoboda, K., Experience-dependent and cell-type-specific spine growth in the neocortex. *Nature*, 2006, **441**(7096), 979–983; http://dx.doi.org/10.1038/nature04783.
8. Kasai, H., Fukuda, M., Watanabe, S., Hayashi-Takagi, A. and Noguchi, J., Structural dynamics of dendritic spines in memory and cognition. *Trends Neurosci.*, 2010, **33**(3), 121–129; http://dx.doi.org/10.1016/j.tins.2010.01.001.
9. Fu, M., Yu, X., Lu, J. and Zuo, Y., Repetitive motor learning induces coordinated formation of clustered dendritic spines *in vivo*. *Nature*, 2012, **483**(7387), 92–95; http://dx.doi.org/10.1038/nature10844.
10. Zuo, Y., Lin, A., Chang, P. and Gan, W.-B., Development of long-term dendritic spine stability in diverse regions of cerebral cortex. *Neuron*, 2005, **46**(2), 181–189; http://dx.doi.org/10.1016/j.neuron.2005.04.001.
11. Oheim, M., Beaurepaire, E., Chaigneau, E., Mertz, J. and Charpak, S., Two-photon microscopy in brain tissue: parameters influencing the imaging depth. *J. Neurosci. Methods*, 2001, **111**(1), 29–37.
12. Theer, P. and Denk, W., On the fundamental imaging-depth limit in two-photon microscopy. *J. Opt. Soc. Am. A Opt. Image Sci. Vis.*, 2006, **23**(12), 3139–3149.
13. Zito, K., Scheuss, V., Knott, G., Hill, T. and Svoboda, K., Rapid functional maturation of nascent dendritic spines. *Neuron*, 2009, **61**(2), 247–258; http://-dx.doi.org/10.1016/j.neuron.2008.10.054.
14. Diaspro, A., Chirico, G. and Collini, M., Two-photon fluorescence excitation and related techniques in biological microscopy. *Q. Rev. Biophys.*, 2005, **38**(2), 97–166; http://dx.doi.org/10.1017/S0033583505004129.
15. Roger, A. W., Tsien, Y. and Ernst, L., *Fluorophores for Confocal Microscopy: Photophysics and Photochemistry*, Handbook of Biological Confocal Microscopy, 2006, 3rd edn, pp. 338–352.
16. Matsuzaki, M., Honkura, N., Ellis-Davies, G. C. R. and Kasai, H., Structural basis of long-term potentiation in single dendritic spines. *Nature*, 2004, **429**(6993), 761–766; http://dx.doi.org/10.1038/nature02617.
17. Xia, W., Zhou, Y. and Shi, M., Advances in two-photon imaging technology. *Zhongguo Yi Liao Qi Xie Za Zhi*, 2011, **35**(3), 204–208.
18. Kobat, D., Horton, N. G. and Xu, C., *In vivo* two-photon microscopy to 1.6-mm depth in mouse cortex. *J. Biomed. Opt.*, 2011, **16**(10), 106014; http://-dx.doi.org/10.1117/1.3646209.
19. Horton, N. G., Wang, K., Kobat, D., Clark, C. G., Wise, F. W., Schaffer, C. B. and Xu, C., *In vivo* three-photon microscopy of subcortical structures within an intact mouse brain. *Nature Photon.*, 2013, **7**, 205–209.
20. Liu, X., Ramirez, S., Pang, P. T., Puryear, C. B., Govindarajan, A., Deisseroth, K. and Tonegawa, S., Optogenetic stimulation of a hippocampal ram activates fear memory recall. *Nature*, 2012, **484**(7394), 381–385; http://dx.doi.org/10.1038/nature11028.
21. Harvey, C. D., Yasuda, R., Zhong, H. and Svoboda, K., The spread of ras activity triggered by activation of a single dendritic spine. *Science*, 2008, **321**(5885), 136–140; http://dx.doi.org/10.1126/science.1159675.
22. Murakoshi, H., Wang, H. and Yasuda, R., Local, persistent activation of Rho GTPases during plasticity of single dendritic spines. *Nature*, 2011, **472**(7341), 100–104; http://dx.doi.org/10.1038/nature09823.
23. Lee, S.-J. R., Escobedo-Lozoya, Y., Szatmari, E. M. and Yasuda, R., Activation of camkii in single dendritic spines during long-term potentiation. *Nature*, 2009, **458**(7236), 299–304; http://dx.doi.org/10.1038/nature07842.
24. Helmchen, F., Fee, M. S., Tank, D. W. and Denk, W., A miniature head-mounted two-photon microscope high-resolution brain imaging in freely moving animals. *Neuron*, 2001, **31**(6), 903–912.
25. Barretto, R. P. J. and Schnitzer, M. J., *In vivo* optical microendoscopy for imaging cells lying deep within live tissue. *Cold Spring Harbor Protocol*, 2012, **2012**(10), 1029–1034; http://dx.doi.org/10.1101/pdb.top071464.
26. Ziv, Y. *et al.*, Long-term dynamics of ca1 hippocampal place codes. *Nature Neurosci.*, 2013, **16**(3), 264–266; http://dx.doi.org/10.1038/nn.3329.
27. Dombeck, D. A., Graziano, M. S. and Tank, D. W., Functional clustering of neurons in motor cortex determined by cellular resolution imaging in awake behaving mice. *J. Neurosci.*, 2009, **29**(44), 13751–13760; http://dx.doi.org/10.1523/-JNEUROSCI.2985-09.2009.
28. Dombeck, D. A., Harvey, C. D., Tian, L., Looger, L. L. and Tank, D. W., Functional imaging of hippocampal place cells at cellular resolution during virtual navigation. *Nature Neurosci.*, 2010, **13**(11), 1433–1440; http://dx.doi.org/10.1038/nn.2648.
29. Dombeck, D. A., Khabbaz, A. N., Collman, F., Adelman, T. L. and Tank, D. W., Imaging largescale neural activity with cellular resolution in awake, mobile mice. *Neuron*, 2007, **56**(1), 43–57; http://dx.doi.org/10.1016/j.neuron.2007.08.003.
30. Dombeck, D. A. and Reiser, M. B., Real neuroscience in virtual worlds. *Curr. Opin. Neurobiol.*, 2012, **22**(1), 3–10; http://dx.doi.org/10.1016/j.conb.2011.10.015.
31. Harvey, C. D., Collman, F., Dombeck, D. A. and Tank, D. W., Intracellular dynamics of hippocampal place cells during virtual navigation. *Nature*, 2009, **461**(7266), 941–946; http://dx.doi.org/10.1038/nature08499.
32. Xu, C. and Webb, W. W., Measurement of two-photon excitation cross sections of molecular fluorophores with data from 690 to 1050 nm. *J. Opt. Soc. Am.*, 1996, **13**, 481–491.